Oxford Open Materials Science, 2022, 2(1): itac001

https://doi.org/10.1093/oxfmat/itac001
Advance Access Publication Date: 2 February 2022
Research Article

RESEARCH ARTICLE

DFT calculations of elastic, electronic and thermal properties of TiB_2Mo

Job W. Wafula [1,*], George S. Manyali[2] and John W. Makokha[1]

[1]Department of Science, Technology and Engineering, Kibabii University, 1699-50200, Bungoma, Kenya and
[2]Department of Physical Sciences, Kaimosi Friends University College, 385-50309, Kaimosi, Kenya

*Correspondence address. Department of Science, Technology and Engineering, Kibabii University, 1699-50200, Bungoma, Kenya. E-mail: jobwafula691@gmail.com

Abstract

Ceramics are materials with good mechanical properties; however, low fracture toughness, intrinsic brittleness and poor resistance against oxidation at high temperatures are challenges limiting their applications. TiB2Mo is a ceramic material whose all elastic properties have not been calculated. In this study, we investigated the elastic, electronic and thermal properties of TiB2Mo structure using first principles calculations. All first principles calculations were based on the density functional theory as implemented in Quantum ESPRESSO code with the help of Thermo_pw as a post-processing code. Obtained lattice parameters of TiB2Mo structure were in good agreement with other previous theoretical studies. TiB2Mo structure was found to be mechanically and dynamically stable at ground state conditions. The results also show that TiB2Mo is brittle, anisotropic and metallic in nature. Based on the calculated Vicker's hardness Hv, we noted that TiB2Mo is classified as a hard material with fracture toughness of above 7 $MPam^{0.5}$; therefore, it is a promising ultra-high temperature ceramic.

Key words: TiB_2Mo; ceramics; elastic properties; electronic properties; thermal properties; density functional theory.

INTRODUCTION

Ceramics are materials of low density with high strength and high elastic moduli. In addition, they have low coefficient of thermal expansion other than excellent resistance against fatigue, creep, corrosion and wear. Some ceramic materials such as TiB_2Mo have a wide range of thermal conductivity as well as the electrical conductivity [1, 2]. Due to their good mechanical properties, ceramics are widely applied not only in the aerospace sector, but also in mechanical engineering for instance internal combustion engines, machine components, thermal management and electronic packaging [3]. These materials are sensitive to impact and they have the ability to absorb kinetic energy through induced large deformation [4]. TiB_2 is one of the suitable candidates of ultra-high temperature ceramic (UHTC) since it exhibits a combination of unique properties. These properties includes high melting point above 3000 K, relatively high hardness of about 30 GPa and strength retention at high-temperature conditions. Other properties are high wear resistance, good thermal and electrical conductivities. Nevertheless, poor fracture toughness of approximately 4 $MPam^{0.5}$, intrinsic brittleness and poor resistance against oxidation at high temperatures are among the challenges facing the applications of ceramic materials [1, 2]. TiB_2-based ceramics have been found to exhibit improved mechanical properties and therefore the current study considered TiB_2Mo ceramic since its all elastic properties have not been calculated. TiB_2Mo is said to have high wear resistance for instance, it was found effective when coated with Steel via electro-explosive deposition method, a high-quality poreless coatings are obtained [5]. Molybdenum (Mo) has been found to be the most suitable and effective element that can improve high temperature-dependent properties of steel and

Submitted: 18 November 2021; **Received (in revised form):** 28 December 2021. **Accepted:** 4 January 2022

high-temperature hardness of the substrate. It was also reported that addition of Mo improves the mechanical properties of a hot-rolled transformation induced plasticity Steel and lastly adding a small amount of Mo enhanced the high-temperature oxidation resistance [6, 7]. In this study, we applied the Density Functional Theory (DFT) as implemented in Quantum ESPRESSO code [8] to compute the elastic properties of TiB_2Mo ceramic material.

COMPUTATIONAL DETAILS

First-principles calculations were based on DFT with the generalized gradient approximation (GGA) parameterized by Perdew, Burke and Ernzerrof (PBE) and the local density approximation (LDA) exchange–correlation functionals as implemented in Quantum ESPRESSO code [9, 10]. Interactions between core electrons and valence electrons were treated within projector augmented wave pseudo-potentials obtained from Quantum ESPRESSO Pslibrary [8]. The valance configurations of Ti, B and Mo atoms considered in this study were $3d^3 3p^2 4s^2 3s^1$, $2p^2 2s^1$ and $4d^3 4p^2 5s^2 4s^1$, respectively. The plane wave energy cut-off (charge density) was set to 75 Ry (600 Ry) for PBE and LDA exchange-correlation functionals. Full geometry relaxation was done to optimize the unit cell, and it was considered completed when the atomic forces were <0.02 eV/Å and pressure <0.5 GPa. TiB_2Mo crystalizes in a 3D simple orthorhombic structure system with space group of Amm2 (38) [11]. The Monkhorst and Pack special k-point sampling method were used to obtain $11 \times 10 \times 4$ meshes for TiB_2Mo structure in the Brillouin zone [12]. Once the optimizations were done, the elastic constants of the TiB_2Mo crystal structure were computed with the help of the Thermo_pw code [13]. Later, other properties such as elastic moduli, Poisson's ratio (n), Pugh's ratio (B/G), Vicker's hardness (H_v), fracture toughness (K_{IC}) and elastic anisotropy were derived from the nine independent elastic constants.

RESULTS AND DISCUSSIONS

Structural properties

GGA and LDA optimized lattice constants (a) 3.083 Å and 3.047 Å, respectively, as indicated in Table 1 are in excellent agreement with previous theoretical studies [11] therefore, the current study is consistent with other studies. It was observed from Table 1 that LDA exchange–correlation functional underestimates the lattice constants of TiB_2Mo and overestimates bulk moduli (B), while GGA-PBE exchange–correlation functional overestimates the lattice constants and underestimates the B.

The TiB_2Mo unit cell was optimized with respect to lattice constants and internal atomic positions to obtain the equilibrium structure indicated in Fig. 1 as visualized by the XCrySDen code [14]. The TiB_2Mo is a 3D structure with bond distances between Ti–B bonds ranging from 2.337 Å to 2.361 Å and for Ti–Mo bond lengths falls within ranges of 2.821–2.917 Å. Mo–B bond lengths range from 2.331 Å to 2.347 Å, whereas all B–B bond lengths are equal to 1.837 Å as indicated in Table 2. Therefore, B–B bonds are the strongest while Ti–B bonds are stronger than B–Mo and Ti–Mo bonds are found to be the weakest since they have the longest bond length.

Table 1: Ground state lattice parameters a (Å), b/a, c/a, volume V (Å^3) and density ρ (g/cm^3) calculated for TiB_2Mo using GGA-PBE and LDA exchange–correlation functionals

XC	a	b/a	c/a	V	ρ
LDA	3.047	1.028	2.736	79.088	6.894
GGA-PBE	3.083	1.031	2.742	82.86	6.629
Others [10]	3.087	1.029	2.738	83.023	6.620

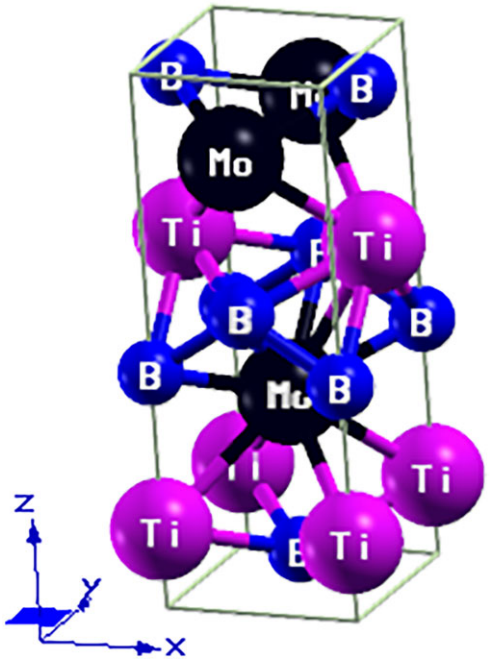

Figure 1: Unit cell of TiB_2Mo.

Table 2: Calculated bond distances between the atoms within TiB_2Mo crystal structure at the ground state conditions

Bond	Bond distance (Å)
Ti1–B6	2.3373
Ti14–B15	2.3617
Ti1–Mo8	2.8215
B3–Mo8	2.3314
B5–Mo8	2.3479
Ti2–Mo8	2.9171
B–B	1.8371

Elastic properties

Elastic constants C_{ij} were obtained by the 'standard' algorithm as implemented in Thermo_pw code. In this method, the code applies the strain to the primitive vectors of the unstrained solid [13]. TiB_2Mo crystal is mechanically stable since the calculated elastic constants C_{ij} presented in Table 3 indicates that the material in consideration satisfies the Born–Huang stability criteria of orthorhombic systems; $C_{11} > 0$, $C_{22} > 0$, $C_{66} > 0$, $[C_{11}+C_{22}+C_{33}+2(C_{12}+C_{13}+C_{23})] > 0$, $(C_{11}+C_{22}-2C_{12}) > 0$, $(C_{11}+C_{33}-2C_{12}) > 0$ and $(C_{22}+C_{33}-2C_{23}) > 0$ [15].

The larger value of the elastic constants C_{ij} the incompressible the material is and therefore greater external force is required to cause deformations on such materials while materials with small values of elastic constants easily undergo deformation [16]. Resistance against linear compressions along [100] and [001] directions is measured by elastic constants C_{11} and C_{33}, respectively. Computed elastic constant C_{11} of TiB_2Mo crystal by both exchange–correlation functionals are higher than C_{33}

Table 3: Calculated ground state elastic constants in GPa and the Kleinman parameter (ς) for TiB_2Mo using GGA-PBE and LDA functionals

XC	C_{11}	C_{22}	C_{33}	C_{44}	C_{55}	C_{66}	C_{12}	C_{13}	C_{23}	ς
LDA	614.72	538.81	617.58	235.92	219.84	268.24	178.79	106.93	147.28	0.9153
GGA-PBE	563.35	496.42	557.50	214.68	205.38	247.19	157.02	96.97	126.53	0.9186

Table 4: Bulk modulus (B), shear modulus (G), Young's modulus (E), and Poisson's ratio (n) calculated for TiB_2Mo using GGA-PBE and LDA functionals

		B (GPa)			E (GPa)			G (GPa)			n	
XC	B_V	B_R	B	E_V	E_R	E	G_V	G_R	G	n_V	n_R	n
LDA	293.01	292.78	292.89	554.43	547.84	551.14	234.01	230.54	232.27	0.1846	0.1881	0.1863
GGA-PBE	264.25	263.85	264.05	509.07	503.92	506.49	215.90	213.22	214.56	0.1789	0.1816	0.1803

Table 5: Computed shear anisotropy factors ($A_{\{100\}}, A_{\{010\}}, A_{\{001\}}$), percent A_B and A_G, universal anisotropy factor A^U, Pugh's ratio, H_v in GPa and fracture toughness (K_{IC}) in $MPam^{0.5}$ of TiB_2Mo using GGA-PBE and LDA functionals

XC	$A_{\{100\}}$	$A_{\{010\}}$	$A_{\{001\}}$	A_B	A_G	A^U	B/G	H_v	K_{ic}
LDA	0.9265	1.0203	1.3480	0.0003	0.0074	0.0760	1.2609	33.20	7.642
GGA-PBE	0.9895	1.0257	1.3290	0.0007	0.0062	0.0643	1.2315	33.26	7.028

which indicates that there are stronger bonds along [100] directions compared to those along [001] direction.

Elastic constant C_{44} is related to the resistance to shear deformation with respect to a tangential stress which is applied to the [100] plane in the [010] direction of a material. Calculated Elastic constant C_{44} is smaller than C_{11} and C_{33} thus suggesting that TiB_2Mo is easily deformed by shear compression along any of the three major directions (x, y and z) of a crystal.

The Kleinman parameter (ς) was computed in order to understand the internal strains as expressed by Equation (1) [17];

$$\varsigma = \frac{C_{11} + 8C_{12}}{7C_{11} + 2C_{12}} \tag{1}$$

The ς provides information about the resistance of a compound against strains due to stretching and bending forces [18]. The derived values of ς of TiB_2Mo as shown in Table 3 depicts the insignificant contribution of bond stretching/contracting to resist the external applied stress. Therefore, mechanical strength in TiB_2Mo is dominated by bond stretching/contracting contributions since the ς is approximately 1.

Elastic constants C_{ij} were used to derive other elastic properties crucial for engineering applications such as bulk modulus (B), shear modulus (G), Young's modulus (E) and Poisson's ratio (n) as given by expression [19];

$$B = \frac{B_V + B_R}{2} \tag{2}$$

$$G = \frac{G_V + G_R}{2} \tag{3}$$

$$E = \frac{9GB}{3B + G} \tag{4}$$

$$n = \frac{3B - 2G}{6B + 2G} \tag{5}$$

The bulk modulus (B) of a material describes the resistance to volume change, whereas shear modulus (G) refers to the measure of resistance to reversible deformations and Young's modulus predicts the stiffness of a material to the change in its length [20, 21]. Calculated Bulk moduli (B), shear moduli (G) and Young's moduli (E) of TiB_2Mo crystal in this study are presented in the Table 4. Young's moduli (E) of TiB_2Mo was observed to be quite larger than the bulk moduli (B) and shear moduli (G) suggesting enhanced stiffness [22]. A number of thermo-physical properties are linked to elastic moduli for instance the Young's modulus (E) and lattice thermal conductivity (K_L) are related by the expression $K_L \sim E$ [23]. Shear modulus (G) of TiB_2Mo is smaller than bulk modulus (B) as indicated in Table 4 implying that mechanical strength of the material in this study is limited by the shear deformation.

Poison's ratio values are 0.1803 and 0.1863 when GGA-PBE and LDA XC functionals are used, respectively, are less than 0.26 as indicated in Table 4 hence TiB_2Mo is brittle [24]. Brittleness was also seen when the Pugh's ratio was computed and values were less than 1.75 as shown in Table 5.

Furthermore, we analysed elastic anisotropy since it is one of the property which determine the inducing of microcraks. For instance the shear anisotropic ratio for the {100} shear planes between the {011} and {010} directions is expressed as [25];

$$A_{100} = \frac{4C_{44}}{C_{11} + C_{33} - 2C_{13}} \tag{6}$$

while the {010} shear planes between {101} and {001} directions;

$$A_{010} = \frac{4C_{55}}{C_{22} + C_{33} - 2C_{23}} \tag{7}$$

and that of the {001} shear planes between {110} and {110} directions given by:

$$A_{001} = \frac{4C_{66}}{C_{11} + C_{22} - 2C_{12}} \quad (8)$$

The shear anisotropic factors of TiB_2Mo computed using GGA-PBE and LDA XC functional in this study are indicated in Table 5. It was found out that the values of shear anisotropic ratio A_{100} and A_{010} are less than 1, while A_{001} is larger than 1 indicating that TiB_2Mo structure is anisotropic in nature. Elastic anisotropy of orthorhombic structures results from the anisotropy of the linear bulk modulus beside the shear anisotropy. The anisotropies of the bulk modulus along the *a*-axis and *c*-axis with respect to the *b*-axis can be expressed as [26]:

$$A_B = \frac{B_V - B_R}{B_V + B_R} \quad (9)$$

and

$$A_G = \frac{G_V - G_R}{G_V + G_R} \quad (10)$$

where B_V and G_V are the bulk and shear modulus from Voigt approximation, while B_R and G_R are bulk and shear modulus from Reuss approximation, respectively.

If A_B=A_G = 0 then the crystal is said to be elastically isotropic while $A_B = A_G = 1$ means the structure exhibits maximum elastic anisotropy property. The calculated values A_B and A_G of TiB_2Mo crystal are shown in Table 5 are seen to be greater than 0 which demonstrates that the TiB_2Mo are anisotropic.

Computed universal anisotropic index is given by the expression [27];

$$A^U = 5\left(\frac{G_V}{G_R}\right) + \frac{B_V}{B_R} - 6 \quad (11)$$

where B_V and G_V are the bulk and shear modulus from Voigt approximation while B_R and G_R are bulk and shear modulus from Reuss approximation, respectively.

Elastic anisotropy index (A^U) of TiB_2Mo crystal was determined and listed in Table 5 shows that TiB_2Mo is anisotropic since the values obtained when both GGA-PBE and LDA XC functionals are used are not equal to zero.

Elasticity or plasticity of TiB_2Mo crystal was analysed by calculating the H_v using Chen's model [28] since it gives results much closer to the experimental data. H_v of a material is given by an expression:

$$H_v = 2\left(\frac{G^3}{B^2}\right)^{0.585} - 3 \quad (12)$$

where *B* and *G* are Bulk modulus and shear modulus, respectively.

The predicted H_v shown in Table 5 implies that the TiB_2Mo is classified as hard since the values are greater than 20 GPa and less than 40 GPa [29]. In addition, we noted that the H_v of TiB_2Mo (33.20–33.26 GPa) is bigger than that of TiB_2 (30 GPa) [1]. This is attributed to the fact that H_v of solid mainly depends on the bond strength of chemical bonding along the *c*-axis [30]. Besides the strong 3-D network of B–B bonds, TiB_2Mo structure has additional strong B–Mo bonds which also contributes to the plasticity or elasticity of the material.

Fracture toughness K_{IC} of TiB_2Mo was calculated using Niu's theoretical model [31] as listed in Table 5. We noted that the predicted value of fracture toughness K_{IC} of TiB_2Mo was larger than that of TiB_2 [1] demonstrating the improved resistance against crack propagation.

Melting point

Melting point T_m is correlated to both bonding energy and thermal expansion of crystalline materials. Materials with lower thermal expansion, higher cohesive energy, higher bonding energy and strong atomic interaction have higher melting points [32]. In addition, melting point of compounds or element can be used to predict the temperature up to which the materials are functional without excessive distortion or changes in chemical composition or undergoing substantial oxidation. The melting point T_m of materials in the current study were predicted by the following equation [33]:

$$T_m = 354K + (4.5K/GPa)\left(\frac{2C_{11} + C_{33}}{3}\right) \pm 300K \quad (13)$$

The predicted melting point of TiB_2Mo is 3124.53 ± 300 K using GGA-PBE while 2880.30 ± 300 K when LDA was used and these findings implies that it is a suitable material for high-temperature applications. The melting point was treated as a rough estimate since there is a large uncertainty (±300 K) and there is no experimental value available at present to compare. When compared with other ternaries compound with high melting point such as the recently disclosed Mo_5PB_2 has a melting point of 2359.62 ± 300 K [34] which is lower than that of TiB_2Mo.

Electronic properties

Phonon dispersion curves of TiB_2Mo were computed along the high symmetry points of the Brillouin zone as shown in Fig. 2. TiB_2Mo is dynamically stable since there are no imaginary phonon frequencies in the calculated phonon spectra [35].

The number of electronic states available to be occupied per unit energy interval is defined by the electronic energy density of states (DOSs). The DOS of a material is a significant parameter which provides necessary information to analyse the contribution of each atom to optoelectronic, magnetic, conductivity properties and more so the bonding characteristics [36]. The calculated DOS profiles of TiB_2Mo presented in Fig. 2 shows that some bands cross the Fermi level, demonstrating the degree of metallicity.

Electronic charge density distribution around the atoms within the TiB_2Mo crystal was calculated since the information is used to analyse the charge transfer among the atoms

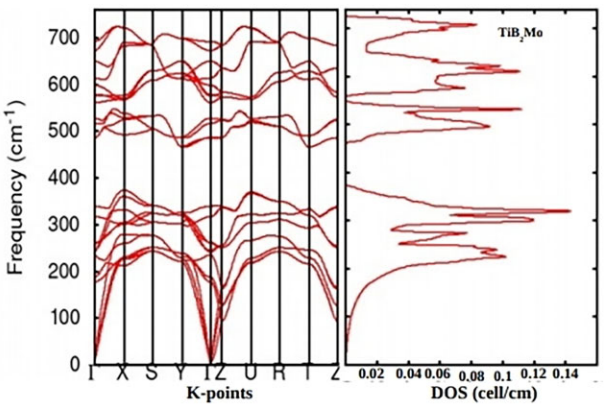

Figure 2: Phonon frequency curves and the DOS of TiB_2Mo.

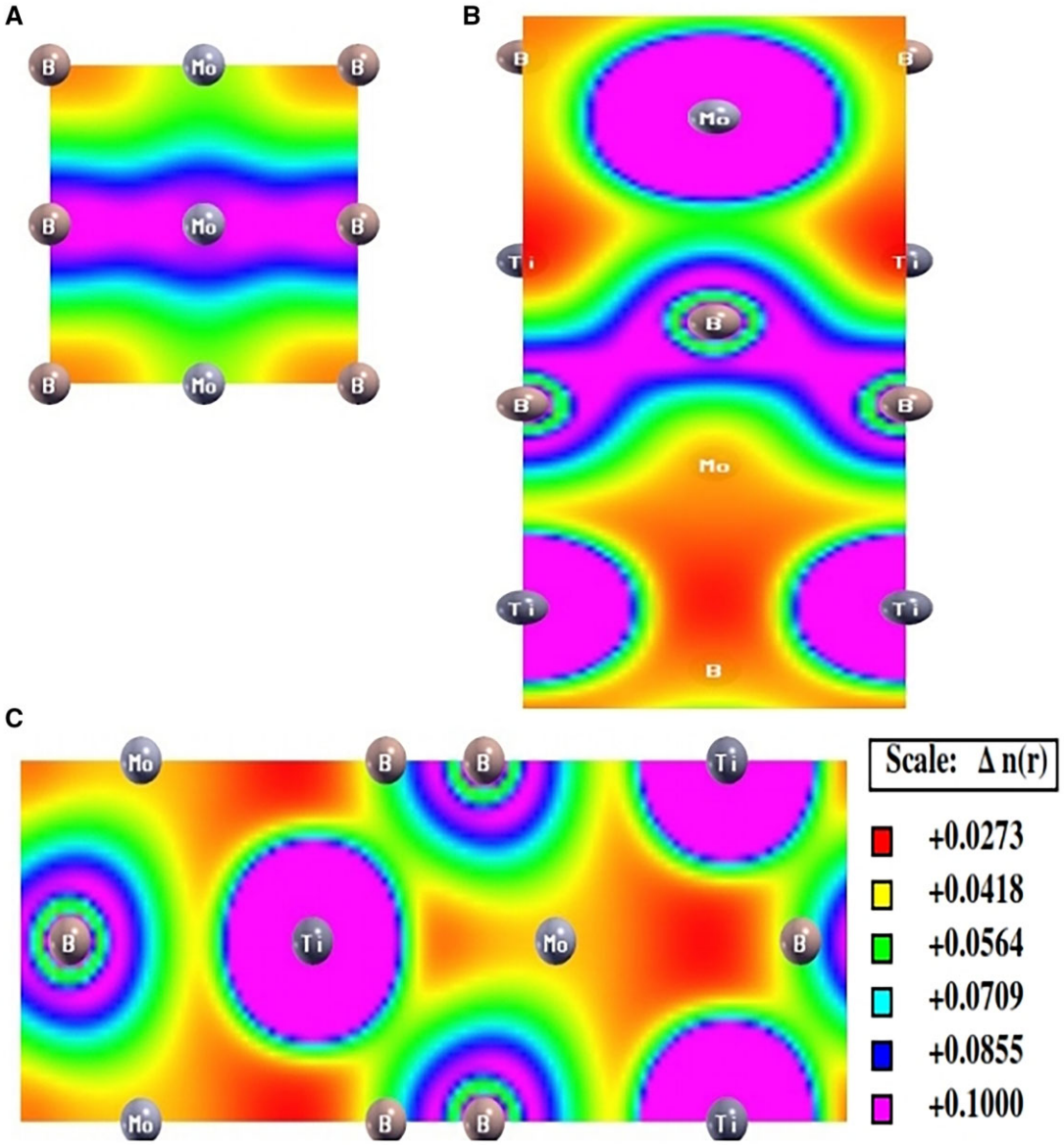

Figure 3: Electron charge density distribution in various crystal planes (a) (001), (b) (010) and (c) (111) TiB_2Mo using GGA-PBE exchange–correlation functional.

material and its chemical bonding characters [37]. The electron charge density of TiB_2Mo crystal in various planes (a) (001), (b) (010) and (c) (111) was computed as shown in Fig. 3. Since pink/purple colour indicates highest electron charge density and red colour indicates lowest electron charge density, therefore, we note that the electron density is greater around the Ti and Mo atoms compared to the B atom. We also observed that electron charge density accumulating around the atomic species were spherical demonstrating significant ionic contribution to the overall chemical bonding in TiB_2Mo crystal. Metallic bonding also contributes to overall chemical bonding since we observed smearing of background charge in TiB_2Mo. Charge density distribution of TiB_2Mo crystal on (001) and (010) planes are different, which shows both direction and plane dependency hence, TiB_2Mo crystal has anisotropic charge density distribution [34]. Generally, we noted that in orthorhombic TiB_2Mo, charge density around the bond B–B > Ti–B > B–Mo > Ti–Mo since we observed earlier that the strength of bond decrease, respectively.

The electronic energy band structure of TiB_2Mo along the high symmetry points in the first BZ was calculated at P = 0 GPa and T = 0 K as presented in Fig. 4. We observed an overlap between valence band and conduction band at Fermi level E_F (E = 0 eV) suggesting TiB_2Mo is metallic nature [35].

Thermal properties

Thermal properties of TiB_2Mo were calculated in the temperature range from 0 to 800 K, since the quasi-harmonic Debye model remains fully applicable within the range. From Fig. 5, it is observed that the Debye Vibrational energy for GGA-PBE and LDA increases non-linearly with temperature especially beyond 200 K contrary to Debye vibrational free energy which decreases with temperature as indicated in Fig. 6.

It is clear from Fig. 7 that the entropy of the TiB_2Mo in orthorhombic phase tends zero at 0 K since stable TiB_2Mo does not exhibit lattice disorder. As temperature increases, TiB_2Mo

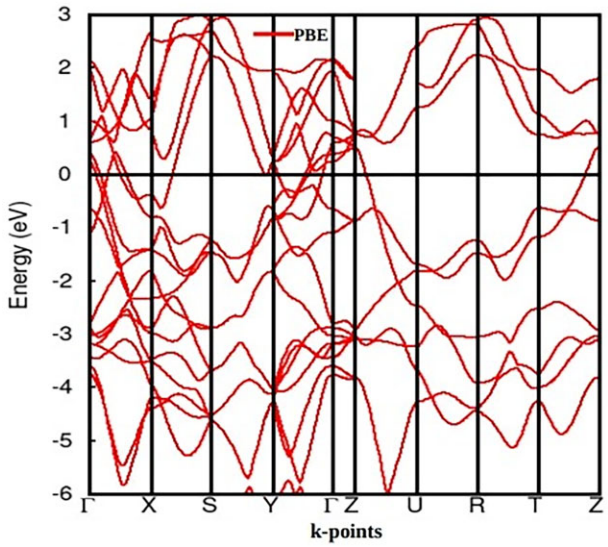

Figure 4: Electron band structure of TiB_2Mo calculated at high symmetry points.

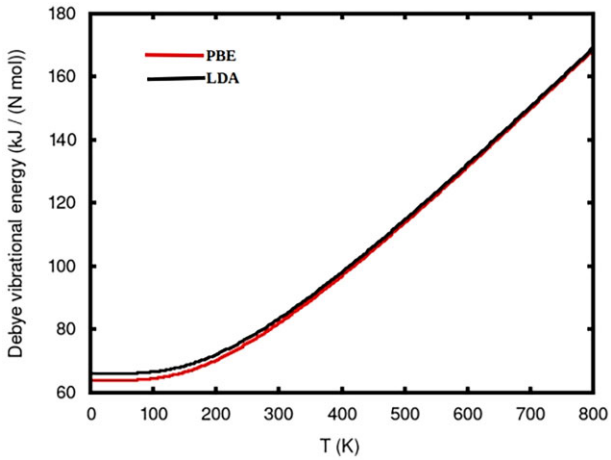

Figure 5: Debye vibrational energy of TiB_2Mo as a function of temperature.

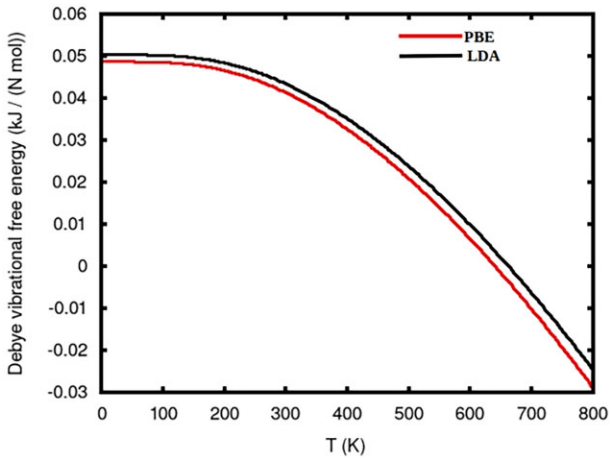

Figure 6: Debye vibrational free energy of TiB_2Mo as a function of temperature.

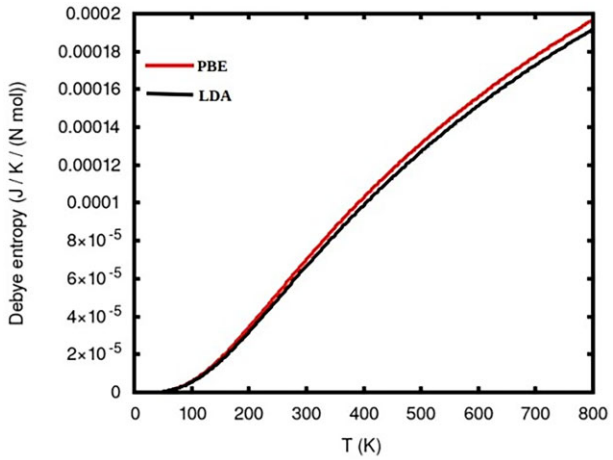

Figure 7: Debye entropy of TiB_2Mo as a function of temperature.

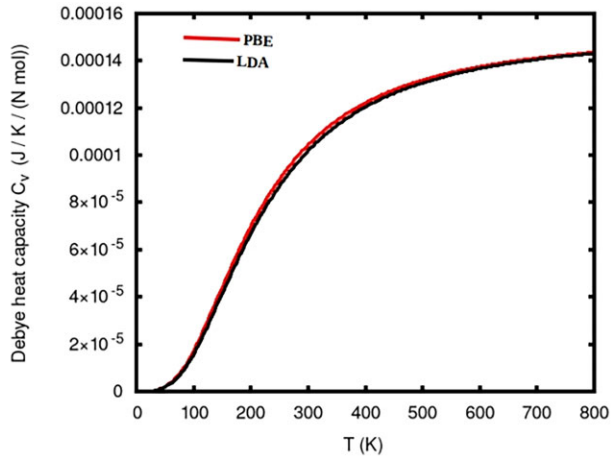

Figure 8: variation of Debye heat capacity with temperature for TiB_2Mo.

system becomes disorderly and explains why the entropy increases with temperature.

Lastly, heat capacity is determined by expression,

$$C_V = (C_V)_{ele} + (C_V)_{pho} \tag{14}$$

where $(C_V)_{ele}$ is heat capacity due to electronic contributions and $(C_V)_{pho}$ is phonon or lattice contribution to the heat capacity. $(C_V)_{ele}$ has a linear dependence on temperature, while $(C_V)_{pho}$ has a cubic dependence on temperature. Figure 8 presents the computed Debye heat capacity (C_V) as a function of temperature (T) TiB_2Mo when both GGA-PBE and LDA XC functionals were used. We observed that $C_V \rightarrow 0$ as $T \rightarrow 0$ for TiB_2Mo which agrees well with the Debye model [38]. TiB_2Mo exhibits cubic dependence on temperature as $T \rightarrow 0$ implying that the phonon contributions is predominant in the orthorhombic phase. Increase in heat capacity with temperature is due to the phonon thermal vibrations and at high temperatures beyond 500 K the anharmonic effect is suppressed hence constant heat capacity approaches the Dulong–Petit classical limit [39]. At low temperatures, heat capacity is directly proportional to T^3 and atomic lattice vibrations rule heat capacity at the intermediate temperatures between 100 K and 500 K.

CONCLUSION

In this work, first principle calculations were used to investigate the elastic, electronic and thermal properties of orthorhombic TiB_2Mo ceramic material. Obtained lattice parameters at ground state were found to accord well other theoretical calculated data indicating the validity of the current study. TiB_2Mo is mechanically and dynamically stable and is classified as hard material with enhanced fracture toughness. We also found out that TiB_2Mo exhibits cubic dependence on temperature since the phonon contributions are predominant in the orthorhombic phase. Lastly, we observed that TiB_2Mo is brittle, anisotropic and metallic in nature. Therefore, we can note that TiB_2Mo has improved mechanical properties suitable for UHTC material.

ACKNOWLEDGEMENT

The author acknowledges the Centre for High-Performance Computing based in Cape Town, South Africa for providing computational resources. We thank Kibabii university for giving us the platform to carry out this research.

FUNDING

There is no funding to disclose.

AUTHORS' CONTRIBUTIONS

J.W.W. conceived the concept, J.W.W. and G.S.M performed first principle calculations using Quantum ESPRESSO software. J.W.W., G.S.M. and J.W.M discussed the results and conclusion. J.W.W. wrote and revised the manuscript.

CONFLICT OF INTEREST STATEMENT

None declared.

REFERENCES

1. Mukhopadhyay A, Raju GB, Basu B. *et al.* Correlation between phase evolution, mechanical properties and instrumented indentation response of TiB2-based ceramics. *J Eur Ceram Soc* 2009;**29**:505–516.
2. Statham G, White S, Adams R. *et al.* Engineering of the magnetized target fusion propulsion system. In: *39th AIAA/ASME/SAE/ASEE Joint Propulsion Conference and Exhibit*, Huntsville, Alabama: Journal of Aerospace information systems. 2003. p. 4526.
3. Zweben, C. Advanced composite materials for optomechanical systems. *Optomechanical Engineering 2013*. Bellingham, WA: International Society for Optics and Photonics, 2013, Vol. **8836**, 883608.
4. Yang M, Qiao P. High energy absorbing materials for blast resistant design. *Blast Protection of Civil Infrastructures and Vehicles Using Composites*. Sawston: Woodhead Publishing, 2010, 88–119.
5. Romanov DA, Budovskikh EA, Goncharova EN. *et al.* Structurally-phase states of electroexplosive composite coatings of the TiB2 Mo system after electron-beam treatment. *Russian Phys J* 2015;**58**;354–360.
6. Wan R, Sun F, Zhang L. *et al.* Effects of Mo on high- temperature strength of fire-resistant steel. *Mater Des* 2012;**35**: 335–341.
7. Zhang M, Luo SX, Liu SS. *et al.* Effect of molybdenum on the wear properties of (Ti, Mo) C-TiB2-Mo2B particles reinforced Fe-based laser cladding composite coatings. *J Tribol* 2018;**140**: 051603.
8. Giannozzi P, Andreussi O, Brumme T. *et al.* Advanced capabilities for materials modelling with Quantum ESPRESSO. *J Phys Conden Matter* 2017;**29**:465901.
9. Perdew JP, Burke K, Ernzerhof M. Generalized gradient approximation made simple. *Phys Rev Lett* 1996;**77**:3865.
10. Baroni S, De Gironcoli S, Dal Corso A. *et al.* Phonons and related crystal properties from density-functional perturbation theory. *Rev Modern Phys* 2001;**73**:515.
11. The Materials Project. Materials Data on TiB2Mo by Materials Project. United States: N. p., 2020. Web. https://doi.org/10.17188/1705901 (30 October 2021, date last accessed).
12. Monkhorst HJ, Pack JD. Special points for Brillouin-zone integrations. *Phys Rev B* 1976;**13**:5188.
13. Dal Corso A. Elastic constants of beryllium: a first-principles investigation. *J Phys Conden Matter* 2016;**28**:075401.
14. Kokalj A. Computer graphics and graphical user interfaces as tools in simulations of matter at the atomic scale. *Comp Mater Sci* 2003;**28**:155.
15. Fan Q, Wei Q, Yan H. *et al.* A new potential superhard phase of OsN 2. *Acta Phys Polon A* 2014;**126**:740–747.
16. Yang R, Shi M, Wei Q. *et al.* A first-principles study of the properties of P-43m-Si3× 2 (X= N, P and as). *Chin J Phys* 2019;**59**: 535–545.
17. Kleinman L. Deformation potentials in silicon. I. Uniaxial strain. *Phys Rev* 1962;**128**:2614.
18. Naher MI, Naqib SH. Structural, elastic, electronic, bonding, and optical properties of topological CaSn3 semimetal. *J Alloys Compound* 2020;**829**:154509.
19. Hill R. The elastic behaviour of a crystalline aggregate. *Proc Phys Soc A* 1952;**65**:349.
20. Kittel C. *Introduction to Solid State Physics, New York, USA: John Wiley & Sons. Eighth Edition*. 2021.
21. Naher MI, Naqib SH. *A Comprehensive Study of the Physical Properties of Nb2P5 Via Ab-Initio Technique*. arXiv preprint arXiv:2103.16027. 2021. https://doi.org/10.1063/5.0047139 (05 May 2021, date last accessed).
22. Hossain MM, Ali MA, Uddin MM. *et al.* Origin of high hardness and optoelectronic and thermo-physical properties of boron-rich compounds B6X (X= S, Se): a comprehensive study via DFT approach. *J Appl Phys* 2021;**129**:175109.
23. Kim W. Strategies for engineering phonon transport in thermoelectrics. *J Mater Chem C* 2015;**3**:10336–10348.
24. Hu WC, Liu Y, Li DJ. *et al.* First-principles study of structural and electronic properties of C14-type Laves phase Al2Zr and Al2Hf. *Comput Mater Sci* 2014;**83**:27–34.
25. Tvergaard V, Hutchinson JW. Microcracking in ceramics induced by thermal expansion or elastic anisotropy. *J Am Ceram Soc* 1988;**71**:157–166.
26. Chung DH, Buessem WR, Vahldiek FW. *et al. Anisotropy in Single Crystal Refractory Compounds*. New York, NY: Plenum, 1968, 328.
27. Ozisik HB, Colakoglu K, Deligoz E. First-principles study of structural and mechanical properties of AgB2 and AuB2 compounds under pressure. *Comput Mater Sci* 2012;**51**:83–90.
28. Chen XQ, Niu H, Li D. *et al.* Modeling hardness of polycrystalline materials and bulk metallic glasses. *Intermetallics* 2011;**19**: 1275–1281.
29. Sangiovanni DG, Chirita V, Hultman L. Toughness enhancement in TiAlN-based quarternary alloys. *Thin Solid Films* 2012; **520**:4080–4088.

30. Pan Y, Wang X, Li S. *et al.* DFT prediction of a novel molybdenum tetraboride superhard material. *RSC Adv* 2018;**8**:18008–18015.
31. Niu H, Niu S, Oganov AR. Simple and accurate model of fracture toughness of solids. *J Appl Phys* 2019;**125**:065105.
32. Naher MI, Naqib SH. An ab-initio study on structural, elastic, electronic, bonding, thermal, and optical properties of topological Weyl semimetal Ta X (X= P, As). *Sci Rep* 2021;**11**:1–21.
33. Parvin F, Naqib SH. Structural, elastic, electronic, thermodynamic, and optical properties of layered BaPd2As2 pnictide superconductor: a first principles investigation. *J Alloys Compound* 2019;**780**:452–460.
34. Naher MI, Afzal MA, Naqib SH. A comprehensive DFT based insights into the physical properties of tetragonal superconducting Mo5PB2. *Results Phys* 2021;**28**:104612.
35. Pan Y, Pu DL, Yu ED. Structural, electronic, mechanical and thermodynamic properties of Cr–Si binary silicides from first-principles investigations. *Vacuum* 2021;**185**: 110024.
36. Pan Y, Guan WM. The hydrogenation mechanism of PtAl and IrAl thermal barrier coatings from first-principles investigations. *Int J Hydr Energy* 2020;**45**:20032–20041.
37. Chen S, Pan, Y. Noble metal interlayer-doping enhances the catalytic activity of 2H–MoS2 from first-principles investigations. *Int J Hydr Energy* 2021;**46**:21040–21049.
38. Kittel C. *Introduction to Solid State Physics*. New York, NY: John Wiley & Sons, 1996.
39. Dulong PL, Petit AT. *Recherches Sur Quelques Points Importans de la Theorie de la Chaleur*. 1819.